Final report to the T-71594 OTKA project
Tamás Ungár
principal investigator of the project

Introduction

In the T-71594 OTKA project we have done (i) synchrotron experiments on Commercial-Purity Titanium (CP-Ti) [15], on the $MgGeO_3$ post-perovskite [23], on hexagonal iron, on plastically deformed Mg and Ti, (ii) laboratory experiments on submicron grain-size Nb and Ta [27], on strongly textured extruded Mg [13,26] and on several multilayer and thin-film specimens of different types and materials [19,20,22,25]. We have published 23 original research papers, 3 review papers and 1 conference proceedings publication, all with the OTKA-71594 number included.

One of the major aims of the project was to work out the evaluation procedure of obtaining the submicron characterization of single-grains from synchrotron experiments on polycrystalline aggregates. We achieved good progress in solving this extremely complex task, comprising of the handling of measurement data of the order of several tens of gigabits. In order to demonstrate this, in paragraph No. 6. we briefly show the preliminary results obtained on Co-Ti and Co-Zr which, however, go beyond the frame of the present project and have not yet been published.

1. Determination of twinning and faulting together with dislocation densities and crystallite size-distributions

Twinning and faulting play an important role in the elastic-plastic response of crystalline materials. This is even more so in the case of hexagonal materials where the limited number of available slip systems with reasonably small Burgers vectors require additional slip modes besides dislocation activity. The effect of twinning and faulting on diffraction profiles, especially its *hkl* dependence, is far more complicated than that of microstrains or crystallite size. Depending on the *hkl* configurations within an *hkl* family, the effect can be (i) broadening, (ii) peak shift or (iii) broadening and peak shift together. In the project we have extended the theory of the effect of twinning in hexagonal materials on X-ray and neutron diffraction patterns [5]. The theoretical results were implemented into the eCMWP software package [5,9,11] and applied to commercial-purity titanium (CP-Ti) [5,15,21] and different Mg alloys [5,13,21,26].

2. The microstructure in strongly textured materials [5,19,20,22,26]

We developed a novel method to evaluate the substructure in individual texture components of strongly textured materials. A systematic procedure was developed to evaluate the density of planar defects together with dislocations and crystallite or subgrain size by X-ray line profile analysis in *fcc* and *hcp* crystals. Powder diffraction patterns were numerically calculated by using the DIFFaX software for intrinsic and extrinsic stacking faults, and twin boundaries for a large number of Bragg reflections up to 20 % fault density. It was shown that the profiles of the sub-reflections are the sum of a symmetrical and anti-symmetrical Lorentzian type functions. About 15,000 sub-reflections were evaluated for their FWHM and their positions relative to the exact

Bragg angle. These values were parameterized as a function of the density and type of planar faults. The whole profile fitting procedure, CMWP, previously worked out for determining the dislocation structure and crystallite size distributions, was extended for planar faults by including these data into the software and is called eCMWP. The method was applied to evaluate twin densities in nanocrystalline and submicron grain size *fcc* specimens and for twinning in different *hcp* materials. More details of the materials, the method and the results obtained during the period of the present project are given in the subsequent paragraphs 2.1 to 2.4.

2.1. The microstructure in strongly textured multilayers [20]

The dislocation density and the Burgers vector population was determined within the Cu and Nb layers in highly-textured magnetron-sputtered Cu-Nb multilayers by X-ray line profile analysis. The measurements were conducted with films on and off the substrates and by orienting the films in the Eulerian cradle for acquiring the *hkl* reflections corresponding to planes of the major texture component. It was found that the dislocation density in the Cu layers does not increase when the layer thickness decreases from 75 to 20 nm. Whereas, the dislocation density in the Nb layers increases slightly when the layer thickness decreases, but does not scale linearly. A vast majority of dislocation population was found to be oriented parallel to the film surface (presumably in the interface plane). If all the dislocations in the as-deposited films are contained in the interfaces, then increasing the layer thickness would result in a linear decrease in dislocation density. The fact that such a linear variation of dislocation density with layer thickness was not observed could be due to a combination of two factors: (i) the density of misfit dislocations in the interface plane gradually increases with layer thickness, and (ii) the density of dislocations within the layers decreases with decreasing layer thickness since dislocations in the layer interior but close to the interfaces are attracted to the interfaces.

2.2. The microstructure in strongly textured nanotwinned thin layers [5,19]

The dislocation density and the average twin boundary frequency was determined quantitatively in as-deposited and cold-rolled nanotwinned Cu thin films by high-resolution X-ray line profile analysis. We found that after cold-rolling the dislocation density increases considerably, whereas the twin boundary frequency decreases slightly. We showed that the quantitative X-ray results are in agreement with earlier transmission electron microscopy observations and microhardness measurements. The increase of flow stress induced by cold-rolling was directly correlated with the average thickness of twin lamellae and the dislocation density in a combined Hall-Petch and Taylor type equation.

2.3. The microstructure in strongly textured columnar thin films [22]

Nanocrystalline Ni thin films were produced by direct current electrodeposition with different additives and current density in order to obtain <100>, <111> and <211> major fiber textures, in the different specimens. The dislocation density, the Burgers vector population and the coherently scattering domain size-distribution was determined by high resolution X-ray diffraction line profile analysis. The substructure parameters were correlated with the strength of the films by using the combined Taylor and Hall-Petch relation, as shown in Fig. 1. The method of the extended convolutional multiple whole profile (eCMWP) procedure was used in a special and novel manner to obtain the substructure parameters in the different coexisting texture

components. A strong variation of the dislocation density was observed as a function of the deposition conditions and was correlated with the strength of the thin films.

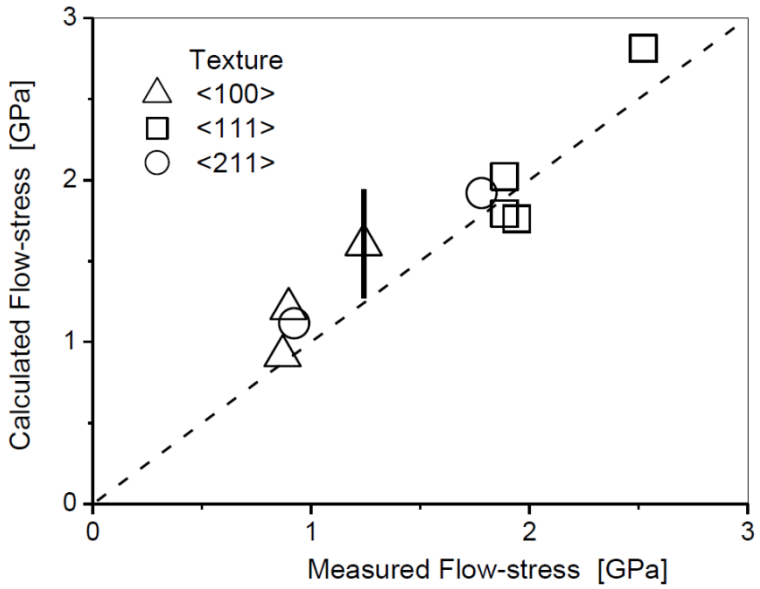

Figure 1. The calculated versus the measured flow stress values for all three different major-textured components. The strength of the foils was measured by Vickers hardness, HV, in a Zwick/Roell-ZHμ-Indentec microhardness tester. The flow-stress was obtained from the HV values as: σ=HV/3. We assumed that the dislocations, the grain size and the twins strengthen the foils by the Taylor and the Hall-Petch mechanisms at the same time. The thick vertical line is for the error bar.

2.4. The microstructure in the different texture components of the strongly textured AZ31-Mg alloy [26]

Tension experiments were carried out at room-temperature, 200 and 400 ^{o}C on AZ31 type extruded magnesium alloy samples. The stress-strain curves are shown in Fig. 2. The absence of an infection in the stress-strain curves indicates that the major work hardening mechanism is dislocation activity. X-ray diffraction patterns provided by a high angular-resolution diffractometer were analyzed in a novel procedure for the dislocation density and slip activity after deformation to fracture in different texture components. The diffraction peaks were sorted into two groups corresponding either to the major or to the random texture components. The two groups of reflections were evaluated simultaneously as if the two texture components were two different phases. The CMWP procedure was modified and developed for this purpose. The dislocation densities in the major texture components are found to be always larger than in the random oriented grain populations. The overwhelming fraction of dislocations prevailing in the samples was obtained to be of <*a*> type with a smaller fraction of <*c*+*a*> type dislocations. The fraction of <*c*> type dislocations was always obtained to be zero within experimental error, in good correlation with earlier TEM observations. The grouping of the different reflections corresponding wither to the major texture component, red bars, or to the random grain populations, blue bars, is shown in Fig. 3. The Lotgering factor is a normalized measure of the peak intensity compared to the random grain orientation specimen.

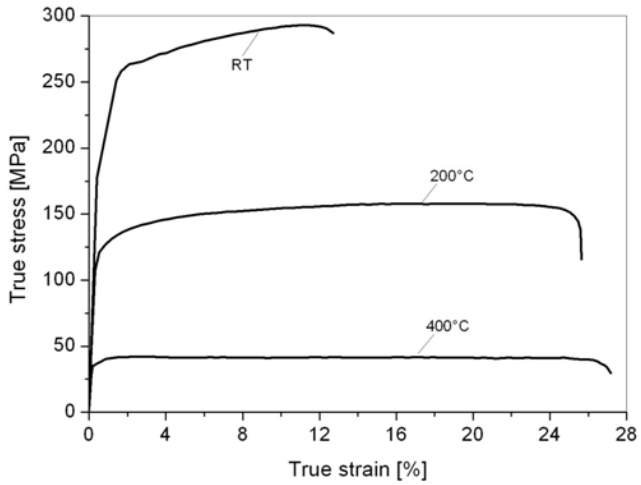

Figure 2. The true-stress true-strain curves of the AZ31 Mg alloy specimens tensile deformed at different temperatures.

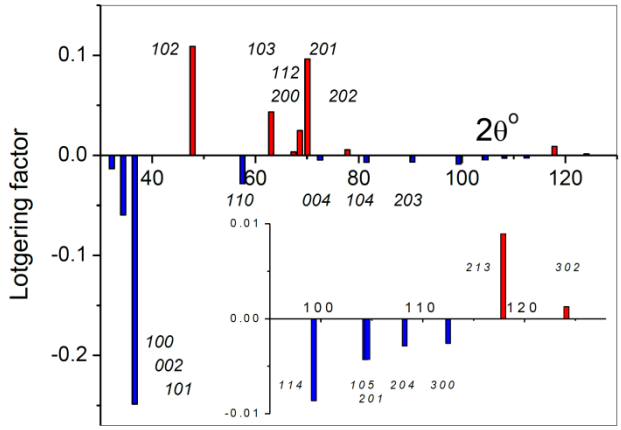

Figure 3. Lotgering-factors of the different *hkl* reflections for the normal-direction (ND) surface of the specimen deformed at RT. The red and blue bars correspond to those *hkl* values for which the Lotgering factor is positive or negative, respectively. The inset in the lower-right corner of the figure is the enlarged part in the 2θ=95 to 128 degree range.

3. The correlation between grain size and dislocation densities in submicron grain size Nb and Ta [13,27]

Niobium and Tantalum are two bcc metals with very different elastic anisotropy. The $A_z=2\times c_{44}/(c_{11}-c_{12})$ constant for Nb and Ta is 0.51 and 1.58, respectively. Submicron grain-size state of the two refractory metals was produced by the method of high-pressure-torsion with different pressure values of 2 and 4 GPa for Nb, and 4 and 8 GPa for Ta, and two different deformations of 0.25 and 1.5 rotations, respectively, with equivalent strains of up to about 40. The dislocation density and the grain size was determined by high resolution diffraction peak-profile analysis. The beam size on the specimen surface was 0.2×1 mm allowing to characterize the sub-structure along the radius of the specimen. The strength of the two metals was correlated

with the dislocation density and the grain size. It was found that, though the grain size is well below 100 nm the role of dislocations in the flow stress of these two metals is significantly larger than that of the grain size. The quasi microdiffraction experiments carried out in the home laboratory are shown schematically by the footprints of the X-ray beam on the specimen at three different positions in Fig. 4. Typical imaging plate (IP) read-outs of the diffraction patterns are shown in Fig. 5. The contribution of dislocations and grain size to the flow-stress are shown in Fig.6. The correlation with the measured and calculated flow stress is shown in Fig. 7.

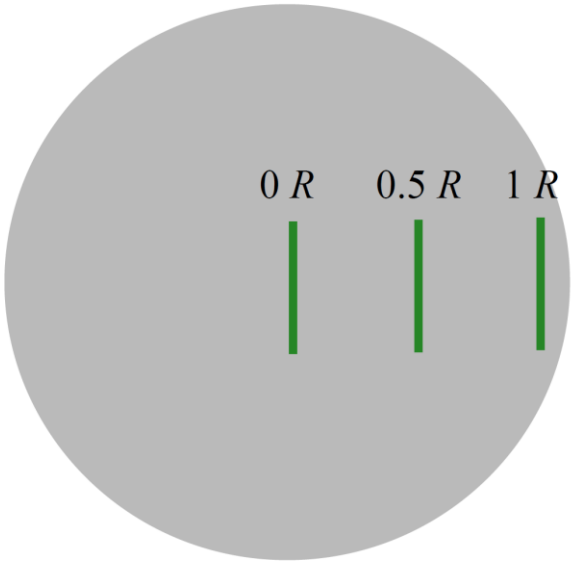

Figure 4. Schematic image of the disc shape specimen of 8 mm diameter with the X-ray beam positions in the center, 0R, at half-radius position, 0.5R and close to the edge, 1R, of the sample. The vertical rectangles are at scale of the footprints of the beam.

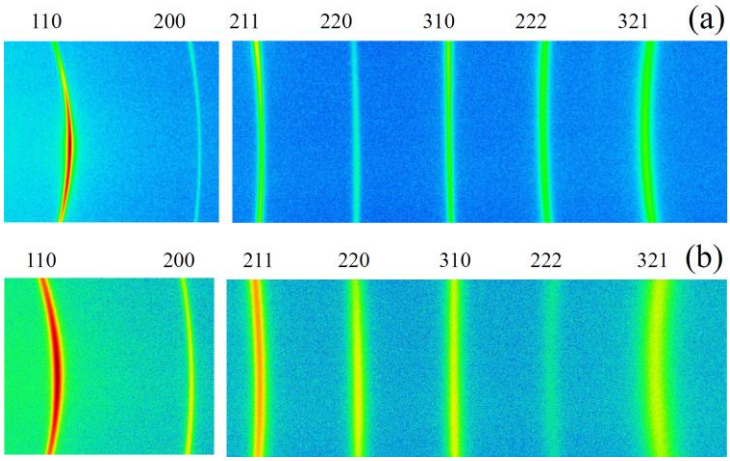

Figure 5. Imaging plate (IP) read-outs of the diffraction patterns for the Nb specimen in the undeformed state (a) and after deformation by 1.5 rotations with 2 GPa pressure (b) measured close to the edge of the disc, i.e. at the R1 position.

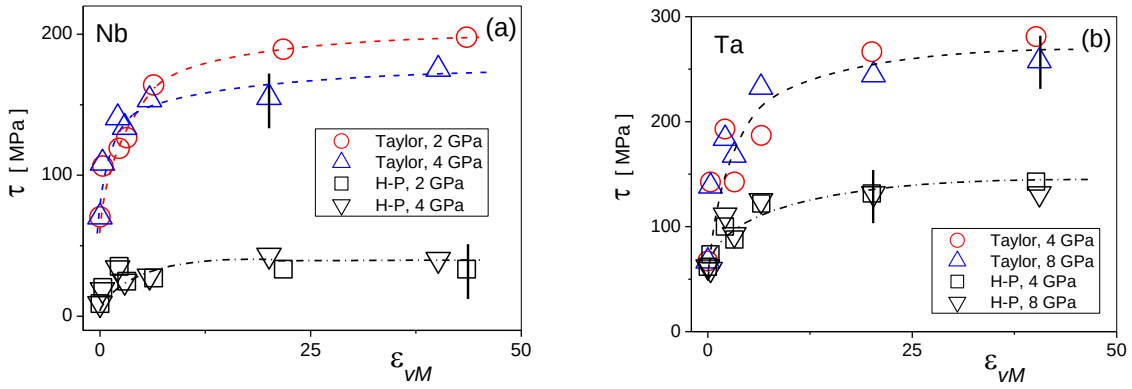

Figure 6. The Taylor type dislocation contributions (blue open triangles or red open circles) and the grain size contributions with the $1/d_X$, reciprocal size dependence (open down triangles or open squares) for the Nb (a) and Ta (b) specimens. Error bars are shown as thick vertical lines.

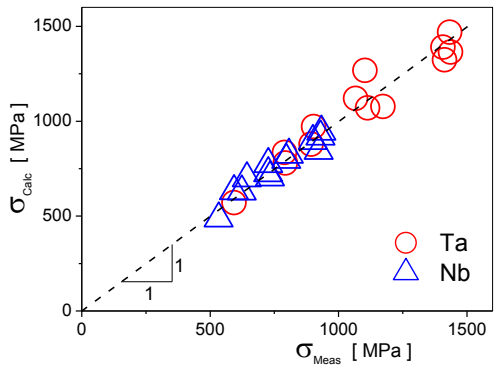

Figure 7. The calculated, σ_{Calc}, versus the measured, σ_{Meas}, flow stress values for Nb (blue open triangles) and Ta (red open circles). Error bars would be equal to the symbol size.

4. Slip-system types in the $MgGeO_3$ post-perovskite [9,11,23]

$MgGeO_3$ post-perovskite (pPv) is a lower pressure analogue of MgSiO3-pPv, which is believed to be the main constituent of the Earth's D″ layer. Understanding the physical properties, especially the stress-strain response of this phase, is critical to explain seismological observations as seismic anisotropy is likely linked to lattice preferred orientation in post-perovskite, which is governed by the motion of defects such as dislocations. Here, we applied in-situ three-dimensional X-ray diffraction to a polycrystalline sample of $MgGeO_3$-pPv at 90 GPa. The specimen was treated in a diamond anvil cell. We could demonstrate that the method can be used to follow individual grain behavior within the material, including the individual orientations, positions, and strain tensors. We used X-ray line profile analysis to characterize dislocations in the grains. We found that the most probable slip systems are either the one with Burgers vectors $1/2\langle 110\rangle$ type gliding on $\{\bar{1}10\}$ or $\{001\}$ planes or the [110](001) slip system. We could not exclude completely the presence of the [100](001) and [001] type dislocations, however, only with a substantially smaller contribution to plasticity. These slip systems are shown to be

consistent with observations of seismic anisotropy in the D″ layer of the Earth's mantle. The schematic setup of the experiment at the ID-11 beamline at the ESRF in Grenoble is shown in Fig. 8. Typical detector images are shown Fig. 9.

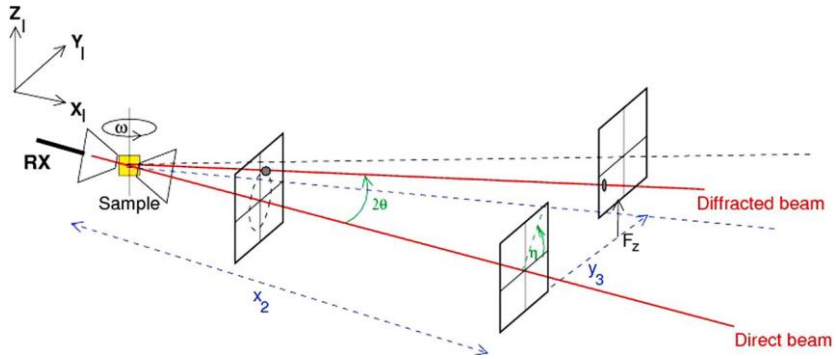

Figure 8. Experimental setup. The sample is confined in a diamond anvil cell on a stage allowing ω-rotation perpendicular to the incoming monochromatic X-ray beam. Data are collected on a flat detector in a close position (x_2 = 152.33 mm) for grain indexation. The detector is then moved to a far position ($x_2 \approx$ 800 mm) and moved sequentially to 7 of the 9 positions of a 3x3 matrix in F_z and y_3 in order to collect the high angular resolution data required for line profile analysis. For each detector position, data are collected while rotating the cell in steps of $\omega = 0.25^o$ in the ω-ranges $80.625^o < \omega < 101.875^o$ and^o $-99.875^o < \omega < -74.125^o$ for the close detector data and for four of the seven far detector positions, and in the w-range $80.625^o < \omega < 101.875^o$ for three far detector positions. This generates 190 and 1018 diffraction images for the close detector and far detector data, respectively.

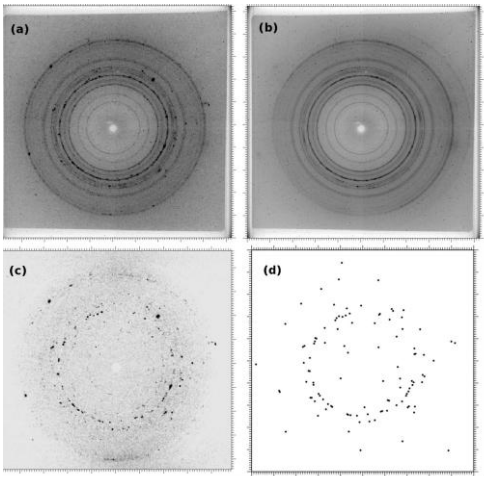

Figure 9. (a) Diffraction image in the close detector position at P = 90 GPa and $\omega = 92.875^o$. (b) Median image calculated for $80.625^o < \omega < 101.875^o$ at P = 90 GPa. (c) Diffraction image shown in Figure 2a with the median removed. (d) Spots extracted from the image shown in Figure 2c.

5. Slip-system types in plastically deformed commercial-purity titanium (CP-Ti) and Mg [9,11,15,]

Burgers vector populations, dislocation types and dislocation densities were determined within individual grains of a polycrystalline commercial-purity titanium specimen by extending a prior

method of differentiating individual grains in a polycrystalline sample. The procedure has been tested at the focused X-ray beamline ID11 at the European Synchrotron Research Facility in Grenoble, France. The results provided by the method can be used as input for different crystal-plasticity calculations and for the experimental verification of numerical simulations.

The thin rod-shape specimen is rotated at a slow rate in the monochromatic X-ray beam over a large ω range while the diffraction pattern is recorded a few hundred times by a fast detector. In the method described in the sample to detector distance is about 200 mm which enables to obtain the diffracted image in a wide reciprocal space range within a relatively short period of time. The specimen diameter and the beam cross-section are adjusted to acquire well separated diffraction spots at one time corresponding to individual grains in the specimen. While the specimen is rotated over the ω axis the diffraction spots are coming-and-going. From the correlation between the ω settings of the specimen and the appearance of the diffraction spots the spots are correlated to specific grains and the grain orientations and positions in the specimen are determined. The method was extended by placing the detector into an additional positions far from the specimen in order to expand the angular resolution for the purpose of line profile analysis [56]. In the far position the detector was moved into several adjacent positions in order to cover a large enough reciprocal space volume. The specimen rotation was repeated for the close and each far detector position.

The evaluation of the diffraction data was carried out in several steps. In the first step the diffraction patterns in the close detector position were indexed and the grain orientations determined. In this procedure the ImageD11 software was used. A typical image provided by this software, once the indexing is successful, is shown in Fig. 10. The Debye-Scherrer rings are straightened. The positions of the Ti reflections according to the 44-1294 ASTM card are indicated by small red + signs. The corresponding indices are given in the figure caption.

The diffraction spots are 3-dimensional intensity distributions in reciprocal space: $I_{hk.l}=I(\eta,\omega,2\theta)$, where η is the azimuth coordinate along the Debye-Scherrer arc, ω is the "rocking-curve" direction and 2θ is the "radial-direction" along the diffraction vector. The microstrain, i.e. the mean square strain $\langle\varepsilon_{g,L}^2\rangle$, produced by dislocations is provided by $I(2\theta)=\int I(\eta,\omega,2\theta)d\eta d\omega$ [5-7]. In the following we call $I(2\theta)$ the *line profile*. The line profile is obtained by integrating the total intensity distribution corresponding to one diffraction spot over η and ω. This procedure was carried out by producing an image recognizing software package which is (i) searching for the cohesive intensity maxima within the consecutive ω frames and (ii) determines the η ranges for the same diffraction maxima in the same ω frames. Once these ω frames and the corresponding η ranges are determined the integration is carried out numerically. Four typical ω frames selected from a cohesive series consisting of altogether 12 frames is shown in Fig. 11. The gray scale images show that the intensity is increasing and decreasing as the corresponding grain comes into and goes out of diffraction orientation. The integration over η is performed within the regions assigned by the black border lines and these results are summed up for each relevant ω frame. A typical diffraction pattern with 5 line profiles is shown in Fig. 12 for one of the grains, #47. Note that some of the line profiles correspond to the same $|\boldsymbol{g}|$ value but to different orientations. The qualitative feature of line broadening can be well seen in the Williamson-Hall (WH) plot of the FWHM values of line profiles. A typical WH plot for grain #44 is shown in Fig. 23a. The data show that the breadths are different for different orientations even for the same $|\boldsymbol{g}|$

values. The diffration profiles were evaluated by the eCMWP method for obtaining the *measured* individual dislocation contrast, $C_{individ}^{Meas}$ factors for each reflection. The last step was to find the dislocation type and Burgers vectors prevailing in the investigated individual grains. This step was carried out by finding the best accordance between the measured and theoretically conceivable, $C_{individ}^{Meas}$ and C_{Theor} dislocation contrast factors. The theoretical contrast factors were determined by using the ANIZC software. The best correlation between the measured and theoretical contrast factors for the grain #44 was found for <*c*+*a*> screw dislocations with the Burgers vector type: <2113>. The qualitative cross-check of the prevailing dislocation type is provided by the *modified* WH plot in which the breadth values are plotted versus $KC^{1/2}$ instead of *K*, as shown in Fig. 13b.

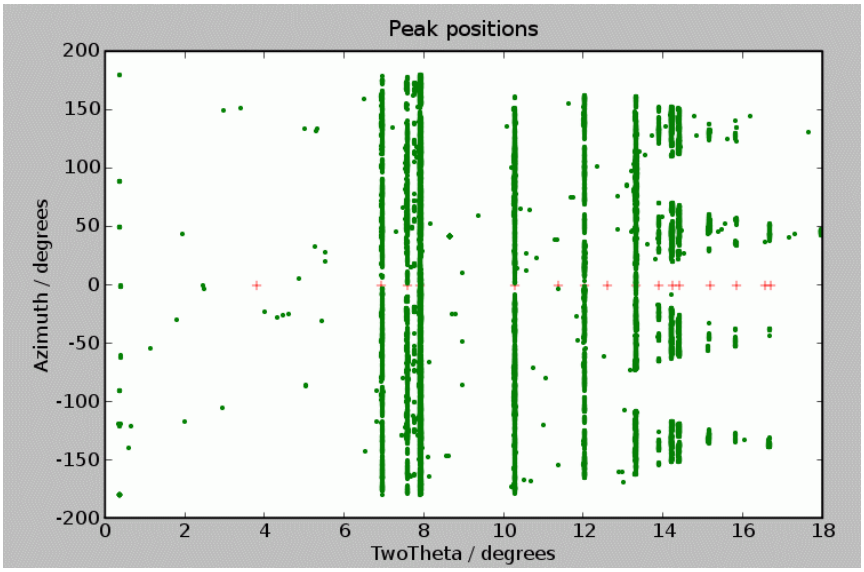

Figure 10. Typical output of the indexing software: ImageD11 once the Debye-Scherrer rings have been straightened. Each spot in the image corresponds to a diffraction maximum. The stray dots are noise which is eliminated in further evaluations. The indices starting from $2\theta=6.9^{o}$ are: 10.0, 00.2, 10.1, 10.2, 11.0, 10.3, 20.0, 11.2, 20.1, 00.4, 20.2, 10.4, 20.3, 21.0 and 21.1. The small red + signs from $2\theta=6.9^{o}$ onward correspond to the first 15 reflections of Ti identified and indexed.

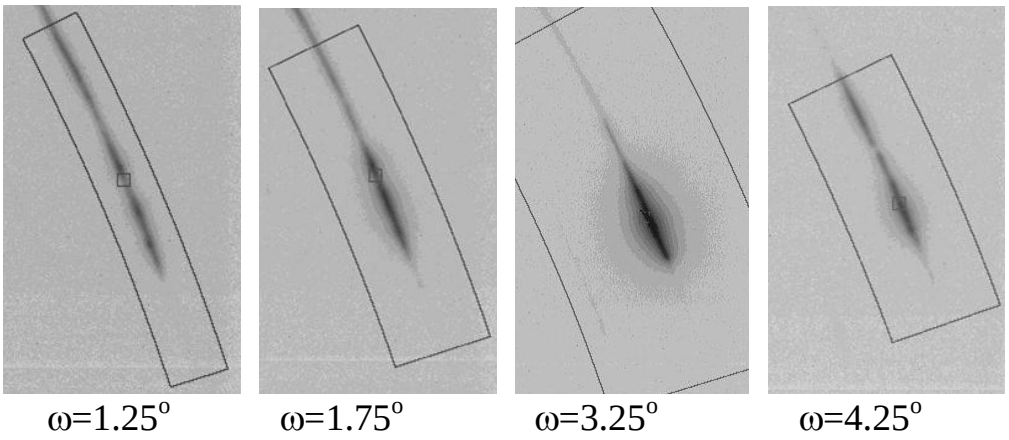

Figure 11. Portions of four typical far-detector frames showing the integration procedure along the Debye-Scherrer arcs in the η direction. The large crosses mark the highest intensity positions in the frames and the lines circumventing the diffraction spots are placed at distances of ±6-times and ±15-times the full-width-at-half-maximum (FWHM) of the peaks in the radial, i.e. 2θ, and in the η directions, respectively. Integration over the ω direction is done by summing up the frames over an ω range where the intensity falls off to 1% of the maximum intensity. For the peak shown here 12 subsequent ω frames have been summed up.

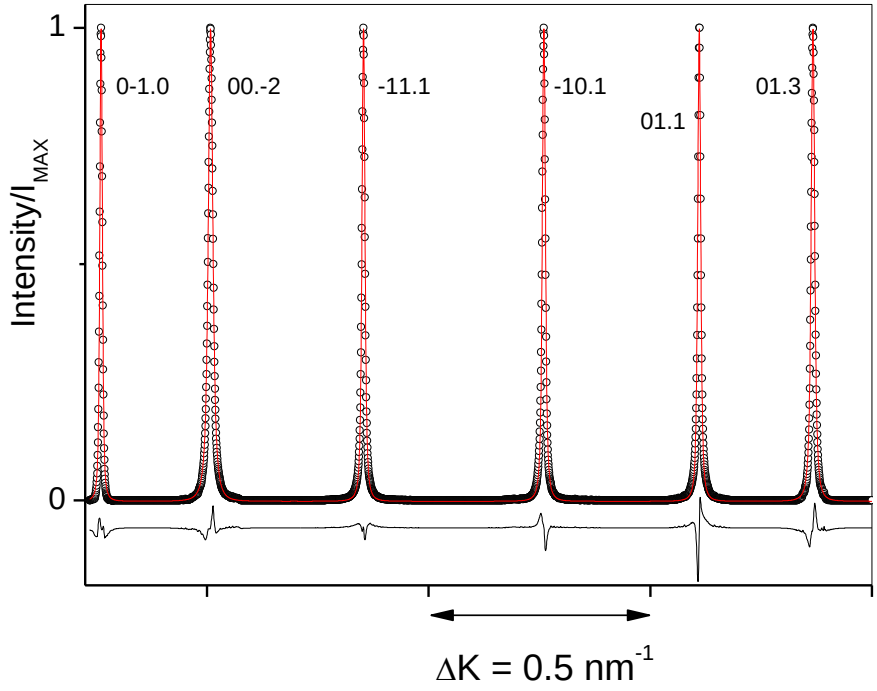

Figure 12. A typical diffraction pattern with 6 line profiles of the grain #47 in a CP-Ti specimen. Note that some of the line profiles correspond to the same $|\boldsymbol{g}|$ value but to different orientations.

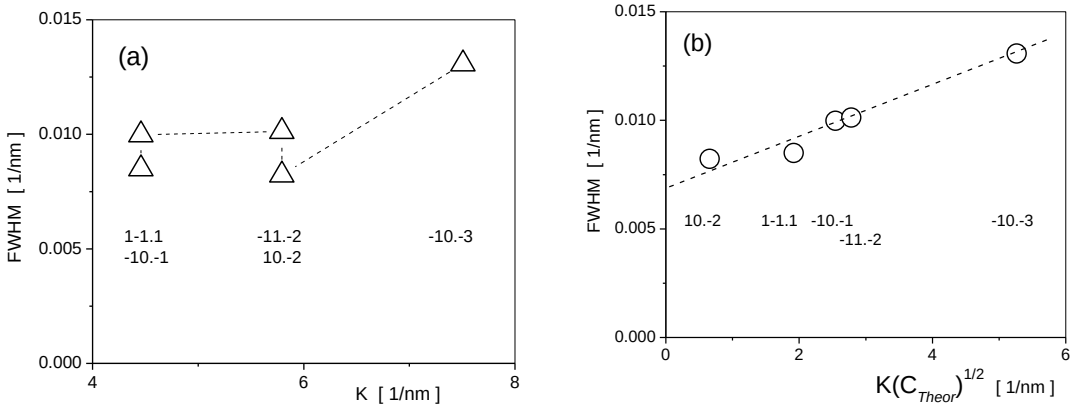

Figure 13. Typical Williamson-Hall (a) and *modified* Williamson-Hall (b) plots for grain #44. The data show that the breadths are different for different orientations even for the same $|\boldsymbol{g}|$ values. In the *modified* Williamson-Hall plot the theoretical dislocation contrast factors correspond to <*c*+*a*> type screw dislocations.

6. Slip-system types in the Co-Ti and Co-Zr alloy systems [9,11]

Please note that the results described in the present paragraph have not yet been published and that they were reached on the basis of the work done within the present OTKA project, however, were achieved after the OTKA project was closed. The purpose to show the results in the present paragraph is to demonstrate that the procedure worked out in the present OTKA project has finally come to a fairly developed stage where these rather complex synchrotron data are handled and processed with good success.

The experiments were carried out at the 1-ID beamline of the Advanced Photon Source synchrotron of Argonne National Laboratory, Argonne, Chicago. Small tapered rod-like polycrystalline samples were made from the plastically deformed Co-Ti and Co-Zr material as illustrated schematically in Fig. 14. The sample was mounted in a one-axis goniometer for rotation over the ω angle during the measurement. The 50 keV monochromatic X-ray beam was focused by a compact refractive lens to an ellipsoidal footprint of the beam on the specimen with horizontal length of about 1 mm and the height between 40 to 100 μm. The scattered radiation was recorded either by a fast high resolution MAR-CCD camera in the close-position at a distance of about 500 mm from the specimen. Or by a GE high-resolution fast solid-state detector in the far-position at a distance of about 2.500 mm from the specimen. In the first run the close-detector was used. The specimen was rotated at small Δω steps and in each step the detector reading was recorded. The total range of ω rotation was 180^o in 1^o steps. In the second run the MAR detector was moved out of the beam and the radiation was recorded in the far-detector position by the GE detector. The specimen was rotated again over ω by the same strategy. The schematic arrangement of the beam, the detectors and the specimen is shown in Fig. 15. In the far detector position the detector was moved successively into six adjacent positions with small overlaps, as indicated schematically in Fig. 15b by the arrows. In each of the detector positions the full measurement cycle with rotating the specimen over ω was repeated. One full measurement cycle consisted of one cycle with the close-detector and six cycles with the far-

detector. Each full cycle took about 6 to 8h beam-time. In order to increase the number of investigated grains the specimens were measured at different heights. Each specimen was measured at four different heights which are called sections. Typical detector images are shown in figures 16 to 18. The first unpublished results are shown in the figures from 19 to 23.

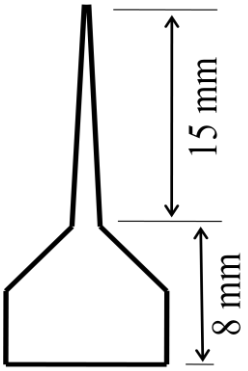

Figure 14. Schematic shape of the tapered specimen. The thick base is for holding it in the goniometer. Tapering is from about 1 mm to a few tens of microns.

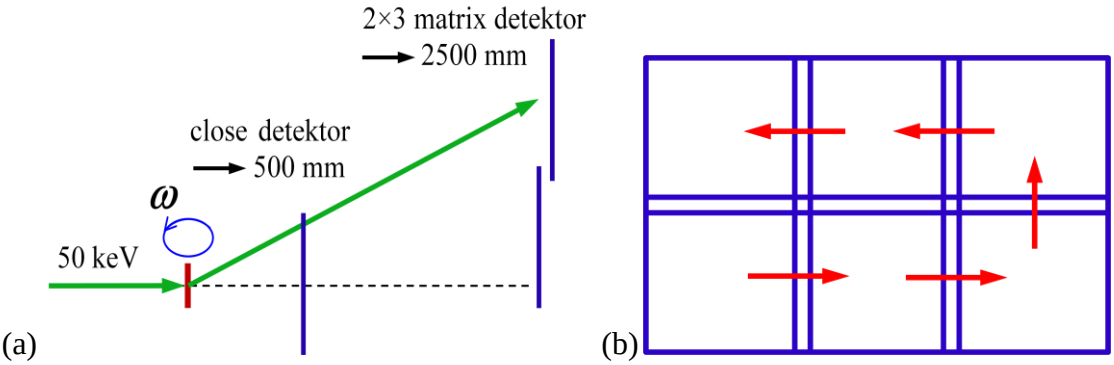

Figure 15. (a) Schematics of the enhanced angular resolution for the purpose of line-profile-analysis with the close and far detector positions. The vertical blue lines indicate the detectors. The short dark rod indicates the specimen rotated over ω. (b) Schematic arrangement of the matrix of the far detector-positions. The small overlap in the detector-positions is also indicated schematically in the figure.

(a) 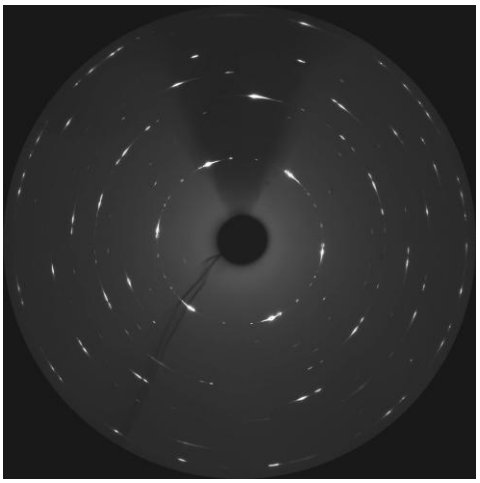 (b) 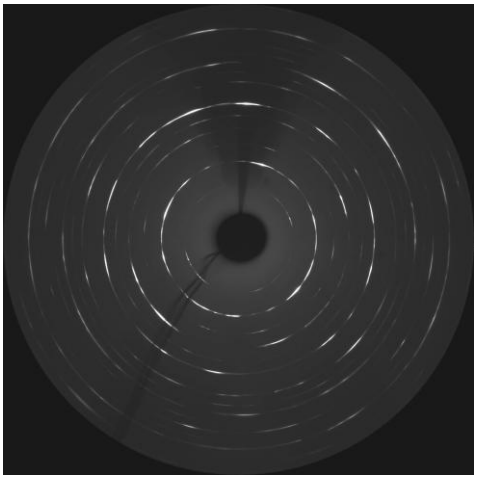

Figure 16. Typical close-detector images of the (a) Co-Ti and (b) Co-Zr specimen.

(a) (b)

(c) (d)

Figure 17. Typical far-detector images of the (a,b) Co-Ti and (c,d) Co-Zr specimen.

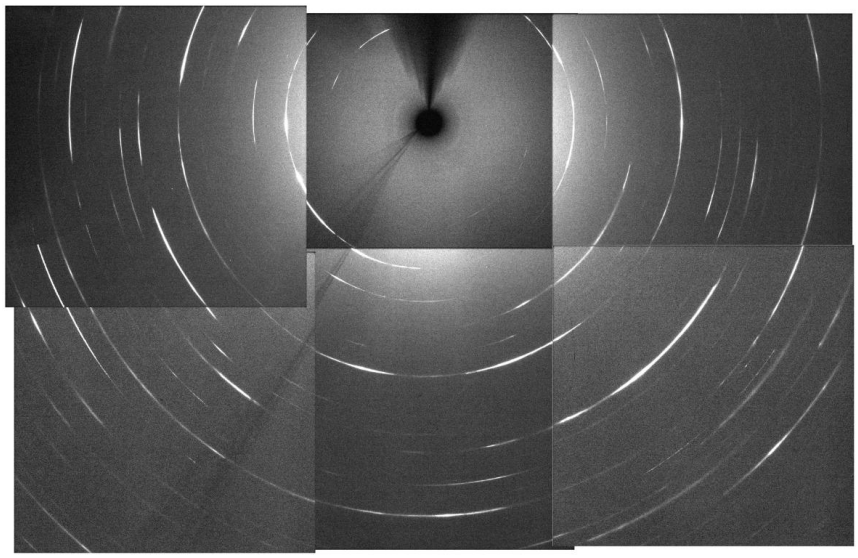

Figure 18. Montage of a far detector image constructed from single frame far-detector images of the Co-Zr specimen, only for the purpose of illustration

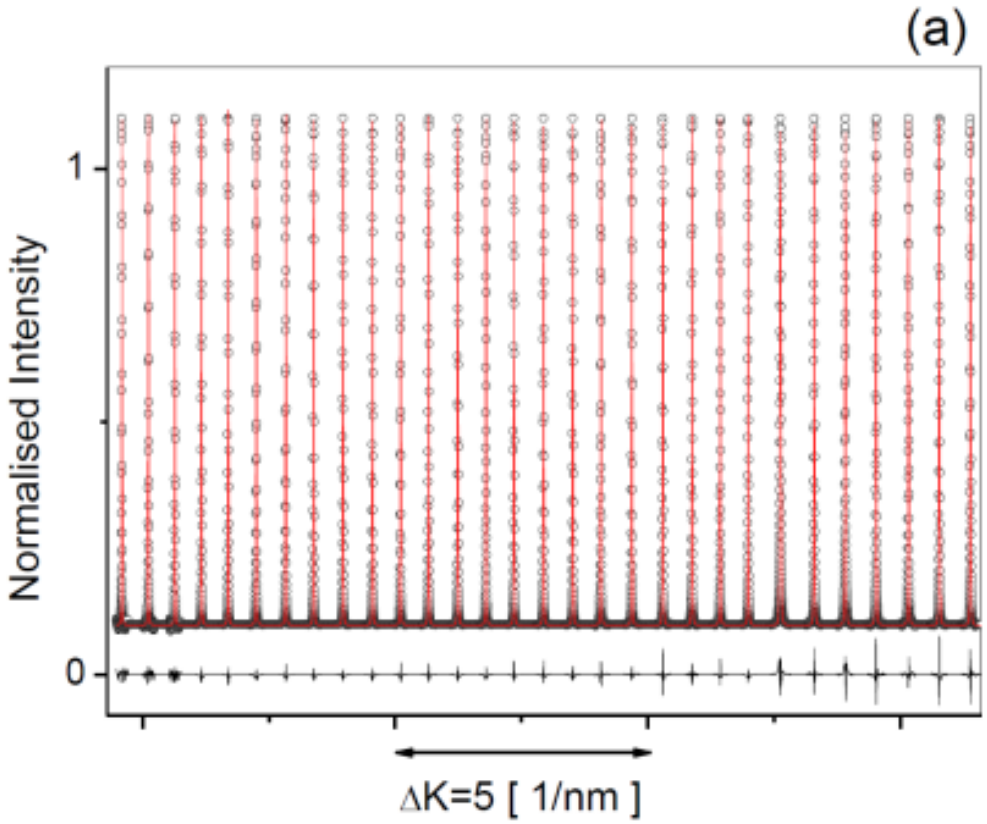

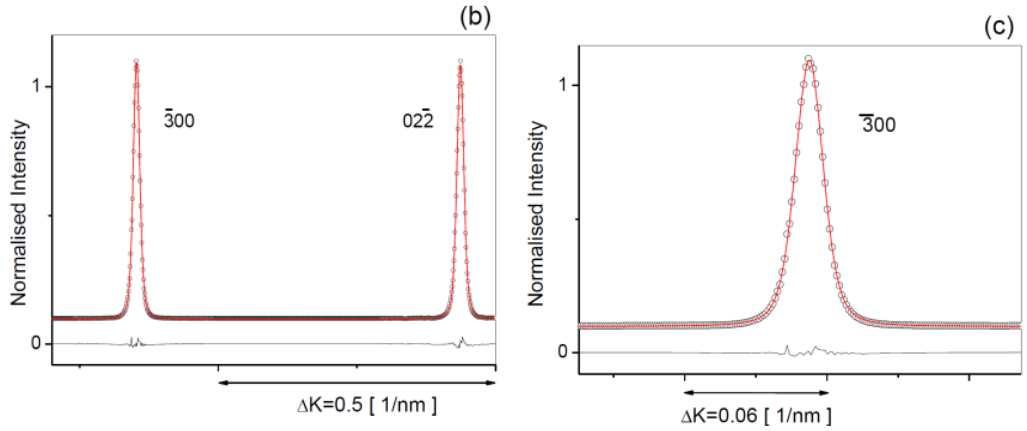

Figure 19. (a) Typical measured diffraction profiles (open circles) corresponding to one particular grain in the Co-Ti specimen. The continuous red line shows the profiles calculated by using the CMWP software package. The black line in the bottom is the difference between the measured and fitted intensities. (b) An enlarged part of the plot showing only 2 reflections and the corresponding *hkl* indices. (c) An enlarged part of the plot showing only 1 reflection. Note that the profiles are put together in a relative ΔK [1/nm] scale, whereas in the CMWP numerical evaluation each profile is treated by using the correct signed *hkl* and the appropriate $K=2\times\sin\theta/\lambda$ values.

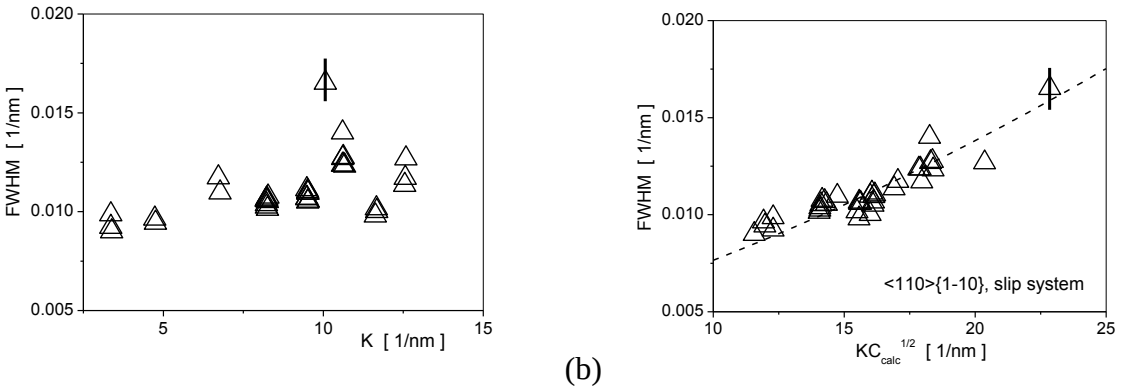

(a) (b)

Figure 20. (a) Typical Williamson-Hall plot of Co-Ti, section-#1 in Grain-#12. (b) *Modified*-Williamson-Hall plot of the same data as in (a).

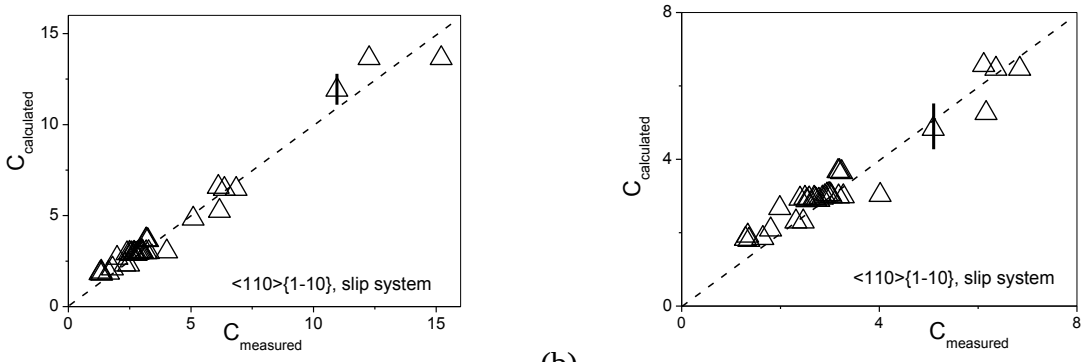

(a) (b)

Figure 21. The correlation between the measured and the calculated dislocation contrast factors, where the calculated values correspond to the <110>{1-10} slip system.
(b) is an enlarged part of (a).

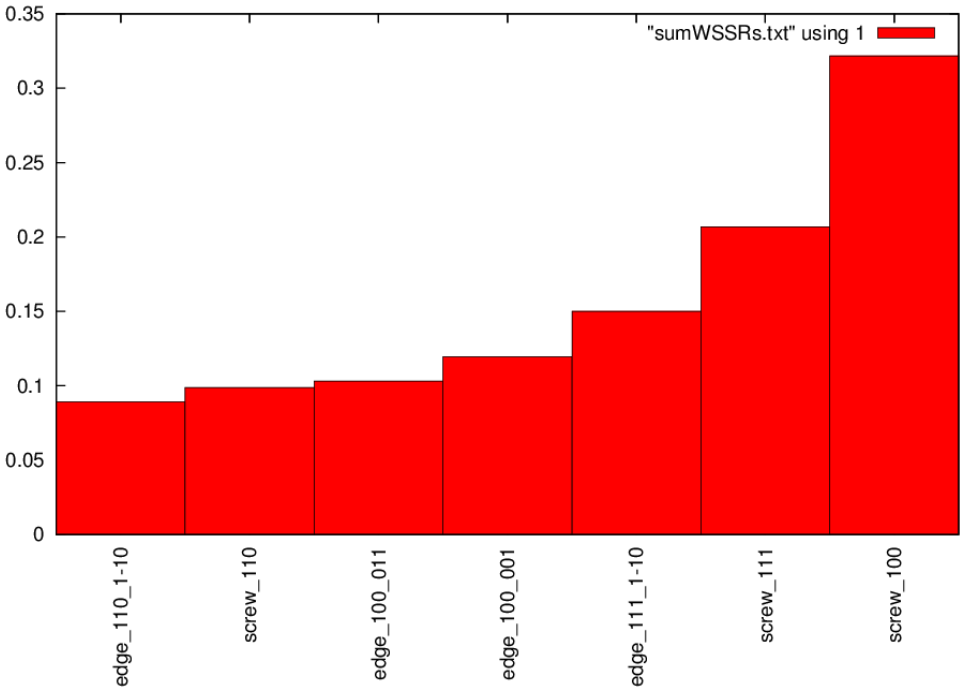

Figure 22. Weighted Sum of Squared Residuals (WSSR) for the matching procedure between measured, C_{meas}, and the theoretical, calculated, C_{calc}, dislocation contrast factors assuming the seven possible dislocation system types in the Grain-#12 in the Co-Ti specimen in section-#1.

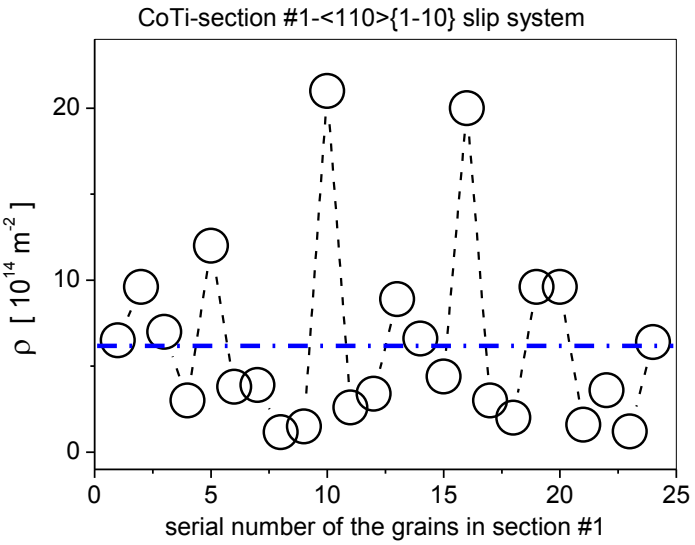

Figure 23. Dislocation densities in the first 25 grains corresponding to the Co-Ti specimen, measured in the first section. The dashed line is only to guide the eye. The blue dash-dot line is the average value $\rho=6.2\times10^{14}$ m^{-2}. The dislocation densities were determined assuming the presence of the <110>{1$\bar{1}$0} slip system with the smallest WSSR in most of the grains.